PHYSICAL REVIEW E **83**, 011115 (2011)

Thermoacoustic waves along the critical isochore

B. Shen and P. Zhang[*]
Institute of Refrigeration and Cryogenics, Shanghai Jiao Tong University, Shanghai 200240, China

(Received 26 August 2010; published 21 January 2011)

Near the liquid-gas critical point, thermal disturbances can generate sounds. We study the acoustic emission over four decades of reduced temperatures [defined as $\varepsilon = (T - T_c)/T_c$, with T_c the critical temperature] along the critical isochore, under linear and nonlinear temperature perturbations, respectively. We identify various thermoacoustic behaviors by numerically solving the governing equations. It is shown that a homogeneous thermoacoustic-wave pattern dominates in the linear case, largely independent of ε; whereas under the nonlinear perturbation, variation in ε could lead to severe wavefront deformation. The strong nonlinear effect is found to be of a transient nature because, in due time, both cases tend to converge in terms of the energy yield of the adiabatic process.

DOI: 10.1103/PhysRevE.83.011115 PACS number(s): 05.70.Jk, 65.40.De, 62.60.+v

I. INTRODUCTION

Thermomechanical interaction is common in compressible fluids at fixed volume. It is predicted that, if heat is added into a confined fluid, the warmed boundary layer will expand and adiabatically compress the rest of the fluid due to the constant total volume. The compression ultimately leads to nearly homogeneous increases in pressure and temperature in the bulk of the fluid. On a shorter time scale, the physical process can be interpreted by the emergence of thermoacoustic-wave motion. In other words, the local temperature change due to the supplied heat can cause transient fluctuations in pressure and density as well on account of the large compressibility; these fluctuations emit sounds. The resulting sound waves, whose propagation is isentropic in nature, then raise the bulk temperature and pressure gradually as they are transmitted in the fluid. An extensive body of literature was devoted to this topic regarding various gases [1–5]. Numerous experiments in gases at room temperature confirmed that acoustic waves could actually be generated as a result of thermal disturbances via this process [6,7]. The effect of thermoacoustic waves on global thermal relaxation, however, was found to be of very limited importance in ordinary gases, in comparison with other mechanisms of heat transport [2]. Near the gas-liquid critical point (CP), fluid properties exhibit drastic changes. In particular, both the isothermal compressibility [$\kappa_T = \rho^{-1}(\partial\rho/\partial P)_T$] and the isobaric thermal-expansion coefficient [$\alpha_P = -\rho^{-1}(\partial\rho/\partial T)_P$] diverge, and the thermal diffusivity ($D = \lambda/\rho C_P$) goes to zero. The thermomechanical effect, therefore, becomes physically more relevant as the CP is neared, to an extent that the dynamics of thermal equilibration can be fundamentally altered as a result. The acceleration of thermalization was first noticed in a microgravity experiment [8], in which the observed time to complete temperature homogenization in supercritical SF_6 turned out to be, quite remarkably, several orders of magnitude less than the ideal heat conduction model predicted. Several groups [9–12] proposed theoretical analyses aimed at rationalizing this anomalous result. The collective conclusion attributed the critical speeding-up to the so-called "piston effect" (PE), which in essence can be viewed as a special case of thermoacoustic coupling. In the close vicinity of the CP, the entropy-based heat transfer matters only inside an ultrathin thermal boundary layer due to the vanishing thermal diffusivity. The extreme compressibility, on the other hand, elevates the thermoacoustic effect to the dominant factor in the bulk temperature homogenization, which is akin to an adiabatic heating effect. As the sound quickly reverberates inside the fluid cell, the temperature change inside the boundary layer can be shared throughout the fluid in an extremely efficient fashion. According to Onuki and co-workers [9,10], the physical time to achieve thermal relaxation close to the CP is represented by the PE time scale,

$$t_{\mathrm{PE}} = \frac{t_D}{(\gamma - 1)^2} = \frac{D^{-1}L^2}{(\gamma - 1)^2}. \tag{1}$$

Here, $t_D = L^2/D$ is the typical diffusion time, with L the characteristic length of the fluid. Since the denominator of the above relation, which includes the adiabatic index γ (namely, the ratio of the specific heats $\gamma = C_P/C_V$), shows a much stronger critical divergence than the numerator, t_{PE} consequently goes to zero on approaching the CP. The existences of the PE and many of its interesting features have since been verified experimentally, in different near-critical fluids [13–19].

As yet, a majority of the research efforts to understand the PE have been focused on its impact on the long-term thermodynamic equilibration, with acoustic characters conveniently filtered out from the process. For instance, extensive research has found that density inhomogeneities caused by rapid thermal equilibration appear to unwind diffusively and slowly [20,21]. Moreover, the extremely high Rayleigh and Grashof numbers near the CP have drawn a lot of interest as well, prompting ample studies on the interaction between gravity-induced natural convection and the PE [22–28]. By contrast, less attention has been directed to examining the acoustic process very close to the CP, which is considered to be the driving mechanism behind the PE [29–31]. Only recently did Miura *et al.* [32] make the first ever experimental observation of the thermally induced acoustic emission. In this paper, we intend to illustrate the evolution of thermoacoustic

---

[*] Author to whom all correspondence should be addressed: zhangp@sjtu.edu.cn

waves across a wide range of temperatures on the critical isochore in the phase diagram, with application of realistic thermophysical properties. On the acoustic time scale (denoted by $t_a = L/c$, with c the sound velocity), the thermoacoustic transients generated by linear and nonlinear temperature perturbations are investigated numerically. It is shown that the distance to the CP plays a twofold role in the development of the acoustic field. In the case of the linear perturbation, the influence of the thermodynamic properties of the fluid is mostly confined to regulating the wave strength; whereas in the nonlinear case, more interesting features related to the degree of criticality are unveiled of the thermoacoustic process.

In Sec. II, the problem formulation and the numerical method employed are introduced. Also presented is the mathematical modeling of the various thermal perturbations of interest, whose effects on the thermoacoustic-wave generation are obtained and analyzed for a wide range of reduced temperatures [defined as $\varepsilon = (T - T_c)/T_c$, with T_c the critical temperature] in Sec. III. Finally, the paper is summarized in Sec. IV.

II. PROBLEM UNDER STUDY

A. The governing equations

We use the full hydrodynamic approach to study the thermoacoustic effect in critical fluids. Mass conservation is represented by the continuity equation,

$$\frac{\partial \rho}{\partial t} + \nabla \cdot (\rho \mathbf{v}) = \mathbf{0}, \tag{2}$$

where ρ is the fluid density and $\mathbf{v}$ is the velocity vector.

The fluid motion is described by the Navier-Stokes equation written for a compressible, viscous, and Newtonian fluid, which reads

$$\frac{\partial (\rho \mathbf{v})}{\partial t} + \nabla \cdot (P\mathbf{G} + \rho \mathbf{v} \otimes \mathbf{v} - 2\eta \boldsymbol{\sigma}) = \mathbf{0}. \tag{3}$$

Here P is the pressure, $\mathbf{G}$ is the metric tensor, and $\otimes$ is the notation for the tensor product. The shear stress tensor $\boldsymbol{\sigma}$ (preceded by the shear viscosity η) denotes the effect of viscous dissipation in the fluid. Note that the bulk viscosity is omitted here. The robust divergence of the bulk viscosity near the CP has been shown to give rise to a second physical regime of the PE [33,34]. On the acoustic time scale, additionally, we have demonstrated that large viscous stresses within the boundary layer are responsible for complex reflection patterns of thermoacoustic waves [35]. The crossover between the classical PE regime and the viscous regime was predicted to occur at $\varepsilon \simeq 2 \times 10^{-4}$ for a 10-mm cell filled with CO_2 [33], and at $\varepsilon \simeq 5 \times 10^{-4}$ for a 1-mm enclosure filled with ^{3}He [34]. The lower bound of the dimensionless temperatures considered herein, $\sim 4 \times 10^{-4}$, falls in a similar vicinity of the CP. We thus expect minimal impact from the bulk viscosity on the relaxation process.

The evolution of entropy in the fluid is described, in the nonconservative form, by

$$\rho T \frac{ds}{dt} = \lambda \nabla^2 T + 2\eta \boldsymbol{\sigma} : \boldsymbol{\sigma}, \tag{4}$$

where s denotes the specific entropy, λ is the thermal conductivity, and $d/dt \equiv \partial/\partial t + \mathbf{v} \cdot \nabla$ is the material derivative. The colon denotes the double tensor contraction. Because of the extremely high compressibility near the CP, the dependence of s on pressure needs to be taken into consideration. Hence, the left-hand side of Eq. (4) is expanded by

$$\begin{aligned} \rho T \frac{ds}{dt} &= \rho T \left[\left(\frac{\partial s}{\partial T} \right)_P \frac{dT}{dt} + \left(\frac{\partial s}{\partial P} \right)_T \frac{dP}{dt} \right] \\ &= \rho C_P \frac{dT}{dt} - \rho \left(C_P - C_V \right) \frac{\kappa_T}{\alpha_P} \frac{dP}{dt}. \end{aligned} \tag{5}$$

Substituting Eq. (5) into Eq. (4), we arrive at

$$\rho C_v \frac{dT}{dt} = \lambda \nabla^2 T + 2\eta \boldsymbol{\sigma} : \boldsymbol{\sigma} - \frac{\rho \left(C_p - C_v \right)}{\alpha_P} \nabla \cdot \mathbf{v}. \tag{6}$$

It should be noted that the third term on the right-hand side of Eq. (6) represents an extra adiabatic temperature change that results from the acoustically driven fluid motion, through which kinetic energy is transformed into thermal energy.

In deriving Eq. (6), a real-fluid equation of state has been used,

$$\delta P = \frac{1}{\rho \kappa_T} \delta \rho + \frac{\alpha_P}{\kappa_T} \delta T. \tag{7}$$

The preceding relation is deemed more appropriate in the neighborhood of the CP than the van der Waals equation of state since it can provide reliable details of the critical fluid behavior.

Equations (2), (3), and (6), supplemented by Eq. (7), constitute the system of governing equations that describe the momentum and energy transport near the CP across different physical time scales. Faced with the onerous challenge of seeking appropriate solutions to these complicated equations, we resort to a high-order finite-difference method. The numerical scheme is based on the explicit MacCormack method, onto which a flux-corrected transport (FCT) algorithm is incorporated to reduce spurious numerical oscillations [36]. In addition, we adopt a theory proposed by Poinsot and Lele [37] to improve the accuracy of numerical simulation near bounding walls.

The results to be presented in Sec. III are obtained with the use of a fine uniform mesh of $\triangle x = 5 \times 10^{-6}$ m and a matching time step of $\triangle t = 2 \times 10^{-10}$ s, through which particularly high spatial and temporal resolution can be realized. In [31,35], we conducted similar numerical studies of the sound generation both close to and far from the CP, in which quantitative comparisons with available experimental data were made and showed excellent agreement.

B. Modeling of the thermal perturbations

Consider near-critical nitrogen confined in a one-dimensional (1D) cell ($L = 10$ mm) that is enclosed by two solid walls. It should be noted that the use of the critical parameters of nitrogen is by no means restrictive. To closely examine the energy conversion involved in the thermoacoustic process (Sec. III C), we will include partial results obtained for near-critical CO_2 for comparison, from which a general pattern can be seen.

TABLE I. Fluid properties for nitrogen with varying ε along the critical isochore.

ε^a	C_v(kJ K^{-1} kg^{-1})	γ(-)	λ(W m^{-1} K^{-1})	α_P(K^{-1})	κ_T(kPa^{-1})	η(μPa s)	c(m s^{-1})
3.96×10^{-4}	1.871	1001.610	0.198	2.826×10^{1}	1.718×10^{-1}	18.773	136.411
3.96×10^{-3}	1.693	101.780	0.087	2.556×10^{0}	1.549×10^{-2}	18.800	144.814
3.96×10^{-2}	1.154	11.960	0.048	1.799×10^{-1}	1.071×10^{-3}	19.061	188.794
3.96×10^{-1}	0.854	2.524	0.037	1.356×10^{-2}	7.941×10^{-5}	21.571	318.538
1.58×10^{0}	0.794	1.660	0.048	3.097×10^{-3}	1.906×10^{-5}	28.761	527.156

[a] Critical coordinates of nitrogen: $T_c = 126.192$ K, $\rho_c = 313.3$ kg/m^3.

At $t = 0$, the fluid is at rest and in perfect thermal equilibrium. The initial conditions are thus given by

$$\begin{gathered} T(x,t=0) = T_i = T_c(1+\varepsilon), P(x,t=0) = P_i, \\ \rho(x,t=0) = \rho_i = \rho_c, u(x,t=0) = 0, \end{gathered} \tag{8}$$

where x refers to the space variable and u is the 1D fluid velocity. The subscript c indicates the critical state. In the present work, to demonstrate the influence of the initial distance to the CP on the acoustic emission, the simulation is carried out for a total of 37 different ε values, spanning from order 10^{-4} to 1 along the critical isochore. Across such a wide range of temperatures, the thermophysical parameters vary considerably (see Table I). For each ε, the fluid is subjected to two different forms of external thermal disturbances, namely, the boundary heating and internal source heating. In what follows, we present their definitions in detail.

1. *The internal source heating*

As Fig. 1(a) shows, a thin continuous heat source located at $x = L/2$ releases its energy at times $t > 0$. The width of the source is $\delta = 25\ \mu$m (which is grossly exaggerated in the figure for illustration purposes). Correspondingly, to the right-hand side of the energy equation (6) should be added a generation term, in the form of

$$q_s(x,t) = \Phi f(x) H(t), \tag{9}$$

where $\Phi = 20$ W/cm^3 is the amplitude of the energy input per unit volume per unit time and $H(t)$ is the Heaviside step function. The spatial configuration of the heat source is described by a dimensionless piecewise equation $f(x)$, which is defined as

$$f(x) = \begin{cases} 1 & \text{if } (L-\delta)/2 \leqslant x \leqslant (L+\delta)/2 \\ 0 & \text{otherwise.} \end{cases} \tag{10}$$

Both the left and right walls are impermeable and thermally insulated at all times, so

$$\begin{aligned} &\frac{\partial T}{\partial x}(x=0,t) = 0, \quad u(x=0,t) = 0, \\ &\frac{\partial T}{\partial x}(x=L,t) = 0, \quad u(x=L,t) = 0. \end{aligned} \tag{11}$$

The problem configuration resembles the immersed film heater used in Miura *et al.*'s experiment [32]. As a result, the simulated thermoacoustic waves based on such a setup exhibit similar features to the experimental observations obtained therein, as will be seen in Sec. III.

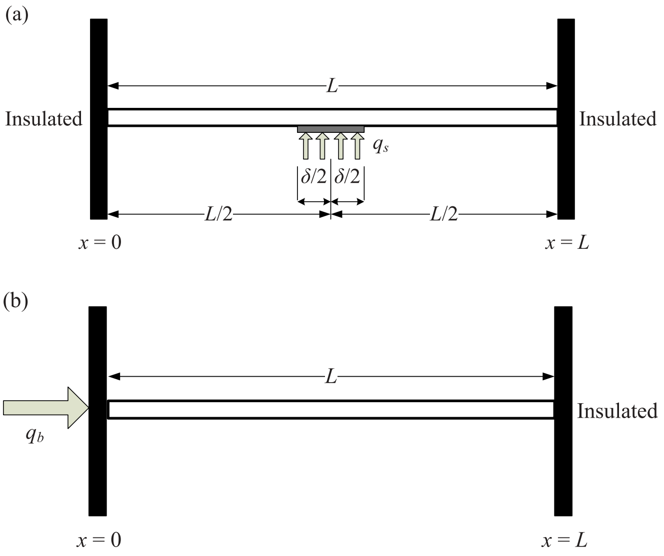

FIG. 1. (Color online) Schematics of the geometry of the fluid cells. At $t > 0$, in (a) a constant heat input of q_s is released into the fluid through a heat source located at $x = L/2$. The width of the source, $\delta = 25\ \mu$m, is small compared with the length of the cell, $L =$ 10 mm. Both walls are thermally insulated. In (b) a constant heat flux of q_b is applied at the left boundary, while the right wall is thermally insulated.

2. *The boundary heating*

Let us now consider, for times $t > 0$, a constant heat flux $q_b =$ 100 W/m^2 imposed on the left end of a 1D slab, whereas the right boundary stays thermally insulated. The problem setup is shown in Fig. 1(b). The boundary conditions are summarized as follows:

$$\begin{aligned} &-\frac{\partial T}{\partial x}(x=0,t) = \frac{q_b}{\lambda}, \quad u(x=0,t) = 0, \\ &\frac{\partial T}{\partial x}(x=L,t) = 0, \quad u(x=L,t) = 0. \end{aligned} \tag{12}$$

Near the CP, particularly large temperature gradients tend to form within the thin boundary layer where thermal diffusion is restrained. One thus expects to find approximately

$$-\left.\frac{\partial T}{\partial x}\right|_{x=0} \simeq \frac{T(x=0,t) - T_{\text{in}}}{\chi_T}, \tag{13}$$

where $\chi_T \simeq (Dt)^{1/2}$ denotes the effective thickness of the thermal boundary layer. On the acoustic time scale, the size of the thermal boundary layer could be extremely small. For instance, at $\varepsilon = 3.96 \times 10^{-4}$, the layer thickness is calculated to be only $8.22 \times 10^{-2}\ \mu$m at $t = 20\ \mu$s. Note that in most circumstances, it is reasonable to assume that the diffusion layer grows as $(Dt)^{1/2}$ uniformly over different time scales [10], but in the viscous regime (corresponding with $\varepsilon \ll 1$), the growth of the boundary layer might cease after reaching the PE time scale [33]. We avoid this region to remove potential ambiguities.

In the above relation, T_{in} is the temperature at the edge of the boundary layer, whose variation in early times is considered very small compared with the boundary temperature increase, and consequently can be omitted. Thus, with the assumption $T_{in} \simeq T_i$, Eq. (13) becomes

$$-\left.\frac{\partial T}{\partial x}\right|_{x=0} \simeq \frac{T(x=0,t)-T_{\mathrm{in}}}{\chi_T} \simeq \frac{T(x=0,t)-T_{\mathrm{i}}}{\chi_T}. \quad (14)$$

Substituting Eq. (14) into the boundary condition (12) and differentiating with respect to t leads to

$$\left.\frac{\partial T}{\partial t}\right|_{x=0} = \frac{q_b}{2\sqrt{\rho C_P \lambda t}}, \quad (15)$$

whose discretized form is employed in our simulation to evaluate the boundary temperature variation [38].

Since thermal diffusion is predominant inside the boundary layer, it is instructive to draw an analogy—as far as the boundary-layer response is concerned—with pure heat conduction. It is illustrated in the appendix that the temperature inside the boundary layer indeed evolves somewhat differently depending on the disturbances, as is suggested in the various analytical solutions. We show in the following that the internal source heating and the boundary heating described above engender in the fluid inherently different thermal perturbations. As a result, the acoustic emission varies notably between the two situations.

III. RESULTS AND DISCUSSION

A. Acoustic emission under the internal source heating

Figure 2(a) shows the temperature ramps at the center of the cell ($x = L/2$) for different initial reduced temperatures ε under the internal source heating. The horizontal axis has been normalized by the acoustic time t_a to accommodate the different thermoacoustic-wave speeds at the different distances to the CP (which are roughly equal to the speeds of sound c). Note that, because the setup is spatially symmetrical, hereafter we redefine $t_a = L/(2c)$ in the case of the internal source heating [see Fig. 1(a)].

As the figure shows, the energy injected at the source leads to a nearly linear temperature rise with time for all ε considered. Analogous boundary-layer behavior can be found in the case of pure diffusion (see the appendix). As thermal diffusion continues to weaken nearing the CP, the heat input appears to induce less pronounced temperature variation as ε decreases. On the other hand, even a small temperature perturbation, due to the diverging compressibility, can in turn result in significant local mechanical imbalance. In Fig. 2(b), we plot the pressure variations at various ε during the same period of time. In sharp contrast to the linear temperature increase, the pressure at $x = L/2$ appears to experience a quasistep jump. Specifically, the rapid pressurization caused by the heating is found to quickly stabilize at a level higher than that in the rest of the fluid, whereby a steady pressure gradient across the boundary layer is created at the locus of heating. Notice that the curves for small ε appear particularly "noisy" with small-scale oscillations, the reason for which is still

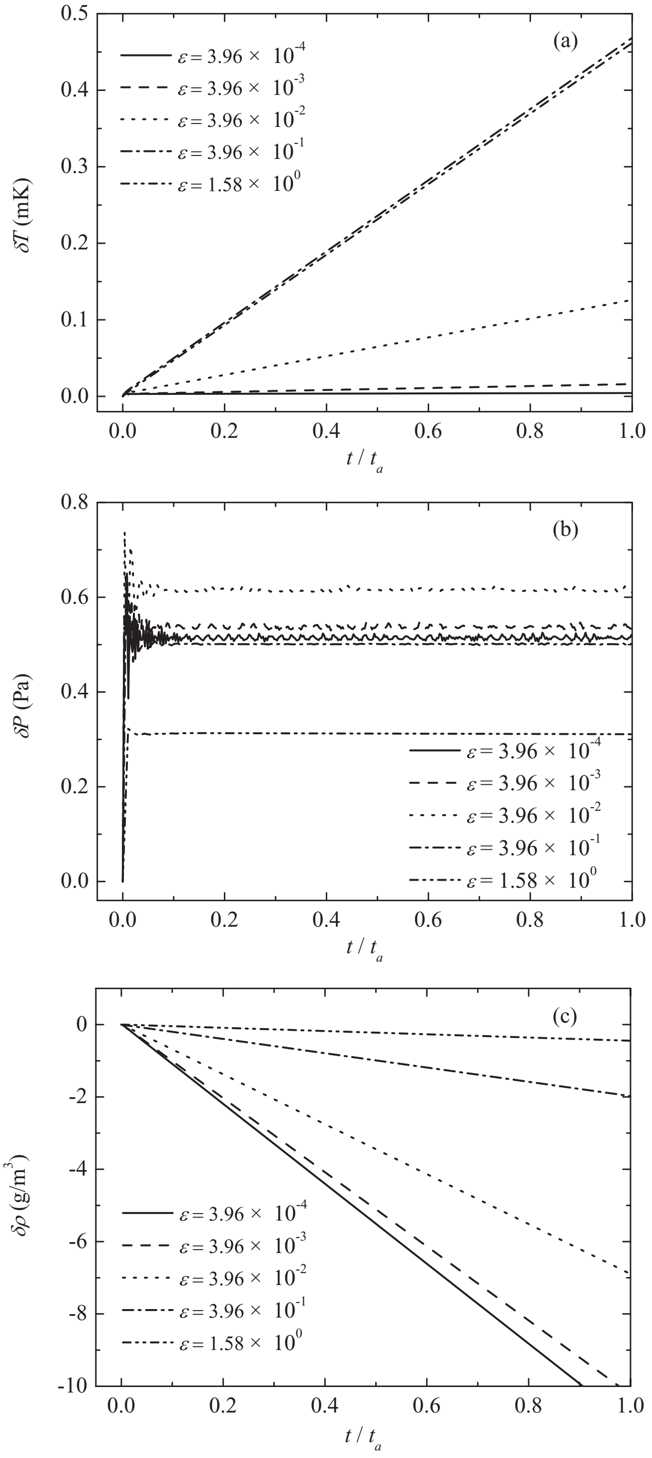

FIG. 2. Temporal evolutions of (a) temperature, (b) pressure, and (c) density at the cell center ($x = L/2$) under the internal source heating. Solid curve: $\varepsilon = 3.96 \times 10^{-4}$; dashed curve: $\varepsilon = 3.96 \times 10^{-3}$; dotted curve: $\varepsilon = 3.96 \times 10^{-2}$; dashed-dotted curve: $\varepsilon = 3.96 \times 10^{-1}$; dashed-dotted-dotted curve: $\varepsilon = 1.58 \times 10^{0}$. The horizontal axes have been scaled by $t_a = L/(2c)$. Notice that the temperatures rise linearly with time at the source in (a).

unclear. One possible explanation is that as the compressibility grows near the CP, the fluid becomes generally unstable, which might in turn increase the risk of possible numerical errors.

Shown in Fig. 2(c) are the density variations at $x = L/2$ resulting from the obvious local pressure buildups [Fig. 2(b)]. Driven by the pressure difference, the fluid starts to flow. As ε diminishes, the expansion becomes markedly stronger. It can be observed that the density at the heat source declines at a growing rate with smaller ε, which is indicative of the increasing thermomechanical interplay on approaching the CP. It should also be noted that, for the time duration considered herein, the heat input seems to have caused mostly minute deviations from the initial equilibrium. By virtue of the equation of state (7), as the pressure remains more or less unchanged [Fig. 2(b)], the temperature-density interaction that is free of noticeable nonlinear effects [Fig. 2(a) and 2(c)] suggests that the boundary layer manages to stay within the critical isochore.

The pressure and density fluctuations [Figs. 2(b) and 2(c)] are capable of generating thermoacoustic waves. In Fig. 3, we draw the temperature distributions at $t = t_a/2$ with various ε. Note that two sound waves of equal strength, traveling in opposite directions, should be emitted from the source in accordance with the symmetrical configuration. For the sake of simplicity, we only show the results in the right half of the fluid cell. It is apparent from the figure that the thermoacoustic-wave features dominate at the early stage of the process. The outstanding temperature gradients located at $x/\mathrm{L} = 0.75$, which is notably far from the thermal boundary layer, divide the cell into a wave region and an undisturbed region. From extremely close to the CP ($\varepsilon = 3.96 \times 10^{-4}$) to some distance off ($\varepsilon = 1.58 \times 10^{0}$), the thermoacoustic waves all assume the shape consisting of a precipitous wavefront and a long flat tail, which complies with the steady pressure surges at the heat source [Fig. 2(b)].

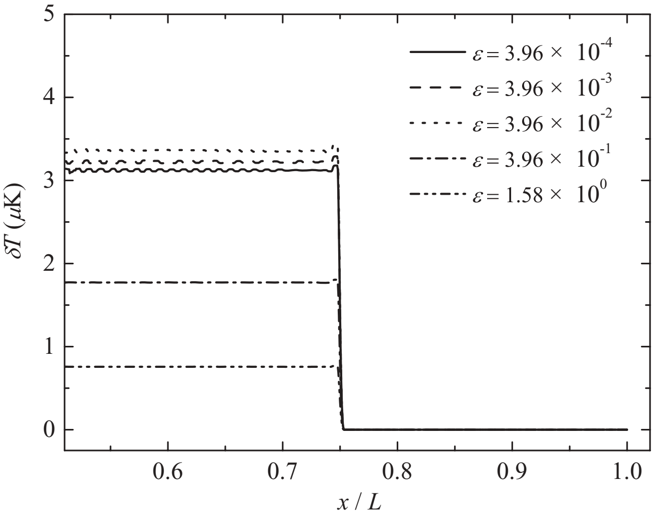

FIG. 3. Spatial temperature profiles at $t = t_a/2$ for various initial reduced temperatures under the internal source heating. Solid curve: $\varepsilon = 3.96 \times 10^{-4}$; dashed curve: $\varepsilon = 3.96 \times 10^{-3}$; dotted curve: $\varepsilon = 3.96 \times 10^{-2}$; dashed-dotted curve: $\varepsilon = 3.96 \times 10^{-1}$; dashed-dotted-dotted curve: $\varepsilon = 1.58 \times 10^{0}$. The horizontal axis has been scaled by L. Homogeneous square waveforms can be clearly observed.

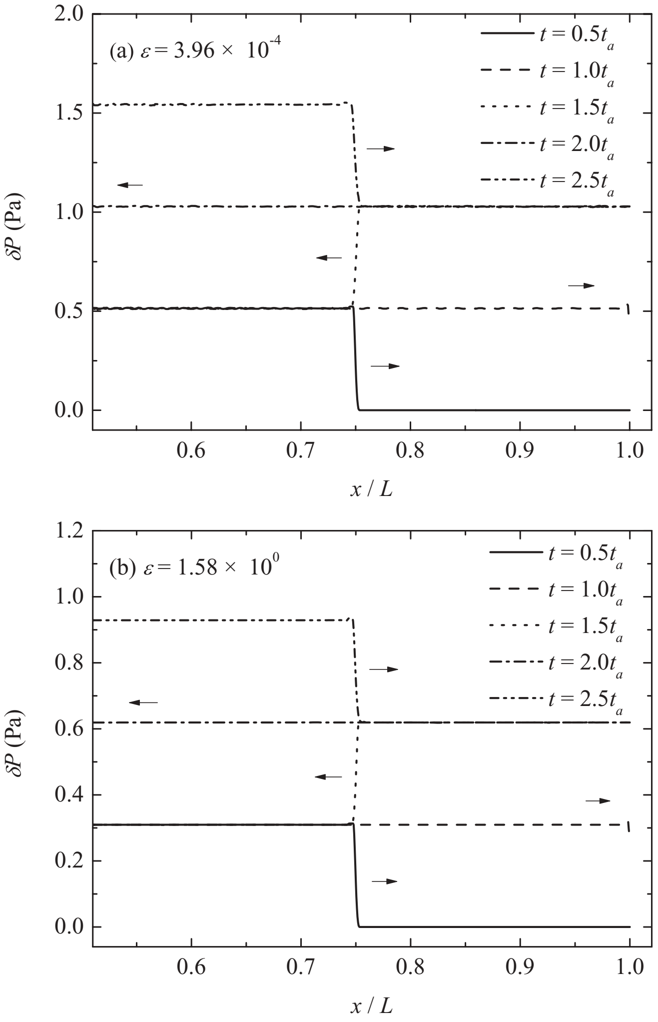

FIG. 4. Spatial pressure profiles at various times under the internal source heating, for (a) $\varepsilon = 3.96 \times 10^{-4}$ and (b) $\varepsilon = 1.58 \times 10^{0}$. Solid curve: $t = 0.5t_a$; dashed curve: $t = 1.0t_a$; dotted curve: $t = 1.5t_a$; dashed-dotted curve: $t = 2.0t_a$; dashed-dotted-dotted curve: $t = 2.5t_a$. The horizontal axes have been scaled by L. The arrows denote the direction of the wave propagation.

The distance to the CP seems to affect only the wave amplitude under the linear temperature perturbation. The subsequent propagation of the thermoacoustic waves is shown in Fig. 4, for $\varepsilon = 3.96 \times 10^{-4}$ and 1.58×10^{0}, respectively. With regard to the relevant acoustic features, the results obtained at the different initial conditions are almost indistinguishable. The bulk pressure, as is suggested in the figure, rises bit by bit through the repeated acoustic transversals between the walls. It is noteworthy that the results reported here exhibit a strong resemblance with the experimentally observed thermoacoustic waves [32], which have been successfully verified analytically and numerically, notably under the assumption of internal source heating [30,35].

B. Acoustic emission under the boundary heating

Recall that through the use of Eq. (15) in modeling the boundary heating, we essentially assign a nonlinear thermal load at $x = 0$ that grows as $t^{1/2}$. In Fig. 5(a) is shown explicitly the $t^{1/2}$ dependence of the boundary temperature at various ε on a log-log scale. Note here the typical acoustic time is $t_a = L/c$.

In Figs. 5(b) and 5(c), we plot the boundary pressure and density variations, respectively, which stand in stark contrast with those obtained under the internal heating [Figs. 2(b) and 2(c)] by exhibiting strong nonlinear features associated with ε. By virtue of Eq. (15), the boundary temperature variation decelerates considerably with decreasing ε, mostly because of the strong divergence of the specific heat C_P near the CP. The initial pressure rise thus becomes gradually dampened as ε diminishes [Fig. 5(b)]. In addition, the rate of the temperature increase also declines as time elapses, according to Eq. (15). Consequently, the boundary pressure is unable to sustain a steady level after the initial increase, as is such with the linear case [see Fig. 2(b)]. Instead we find that the pressure starts to drop after peaking, which happens with a growing delay approaching the CP. It is also suggested in the curves for $\varepsilon = 3.96 \times 10^{-1}$ and 1.58×10^{0} that the boundary pressure could eventually stabilize, apparently at a faster rate with larger ε, as the slackened temperature increase is finally being matched by a commensurate slowing down of the density decrease. As Fig. 5(c) shows, increasingly less flow is generated at the site of heating further from the CP.

Figure 6 illustrates the thermoacoustic waveforms along the critical isochore obtained at $t = t_a/2$ under the boundary heating. Compared with their counterparts with the same ε under the internal heating (Fig. 3), significant wavefront distortions stand out. The nonlinearity shown in the boundary pressure variation is responsible for such prominent differences. For small ε, the slowly varying pressure at the boundary [Fig. 5(b)] produces a dull and smooth wave profile; whereas with very large ε, the transient strong pressure fluctuation [Fig. 5(b)] generates a steep, even shockwave-like wave shape. As is

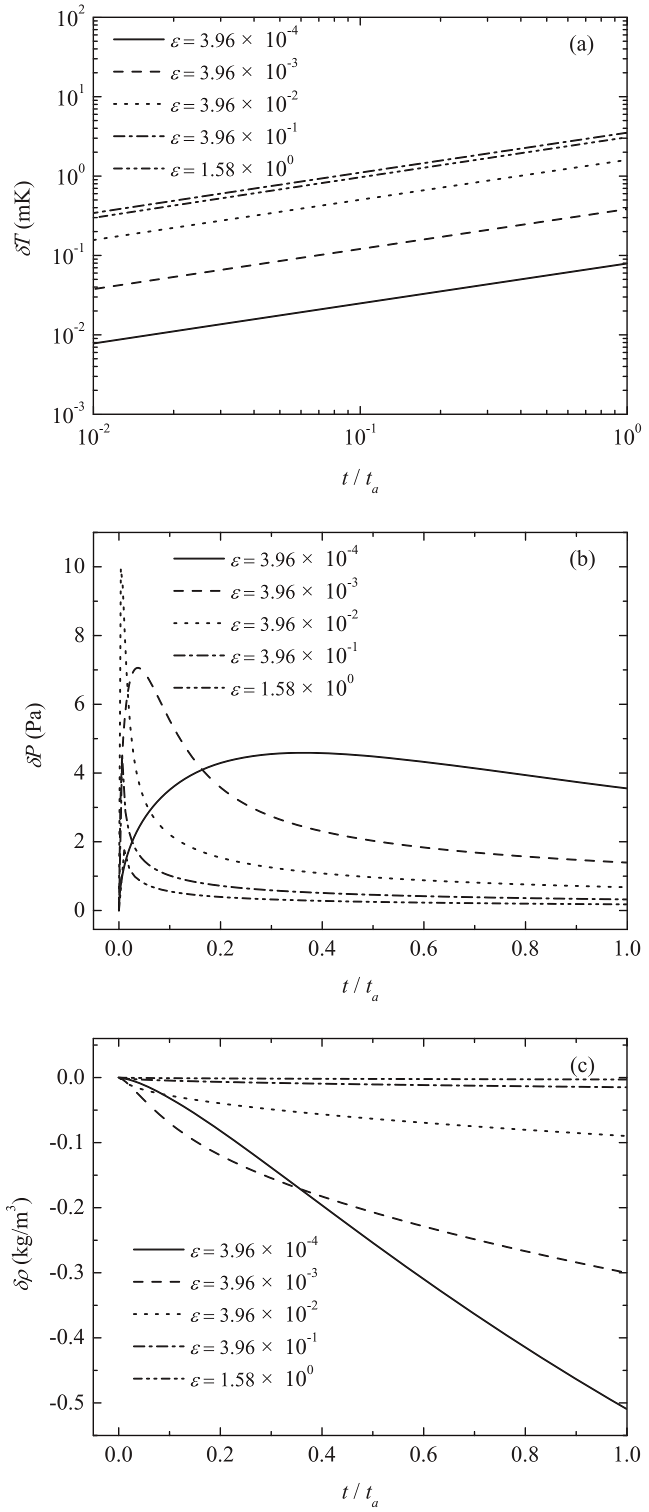

FIG. 5. Temporal evolutions of (a) temperature, (b) pressure, and (c) density at the left boundary ($x = 0$) under the boundary heating. Solid curve: $\varepsilon = 3.96 \times 10^{-4}$; dashed curve: $\varepsilon = 3.96 \times 10^{-3}$; dotted curve: $\varepsilon = 3.96 \times 10^{-2}$; dashed-dotted curve: $\varepsilon = 3.96 \times 10^{-1}$; dashed-dotted-dotted curve: $\varepsilon = 1.58 \times 10^{0}$. Here the horizontal axes have been normalized by $t_a = L/c$. In addition, the results for the temperature variations are presented on a log-log scale. Note that the boundary temperatures show a growth as $t^{1/2}$ in (a). Strong nonlinear effects can be observed in the pressure variations in (b) and the density variations in (c) in connection with ε.

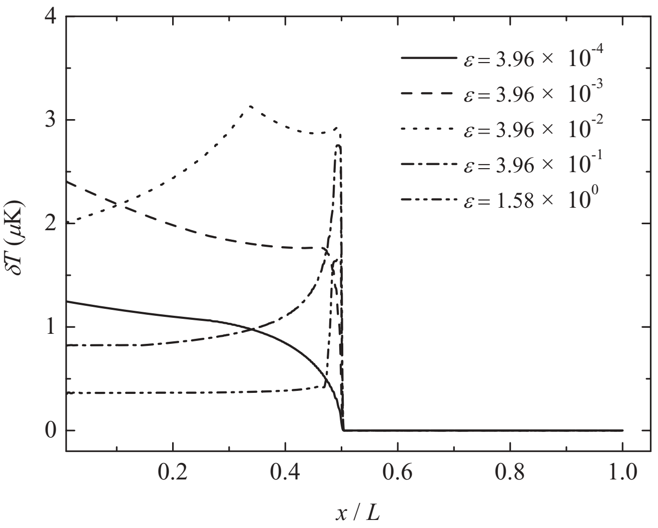

FIG. 6. Spatial temperature profiles at $t = t_a/2$ for various initial reduced temperatures under the boundary heating. Solid curve: $\varepsilon = 3.96 \times 10^{-4}$; dashed curve: $\varepsilon = 3.96 \times 10^{-3}$; dotted curve: $\varepsilon = 3.96 \times 10^{-2}$; dashed-dotted curve: $\varepsilon = 3.96 \times 10^{-1}$; dashed-dotted-dotted curve: $\varepsilon = 1.58 \times 10^{0}$. The horizontal axis has been scaled by L. The wavefront profiles vary significantly with ε, from a smooth gradual rise to a short steep fluctuation.

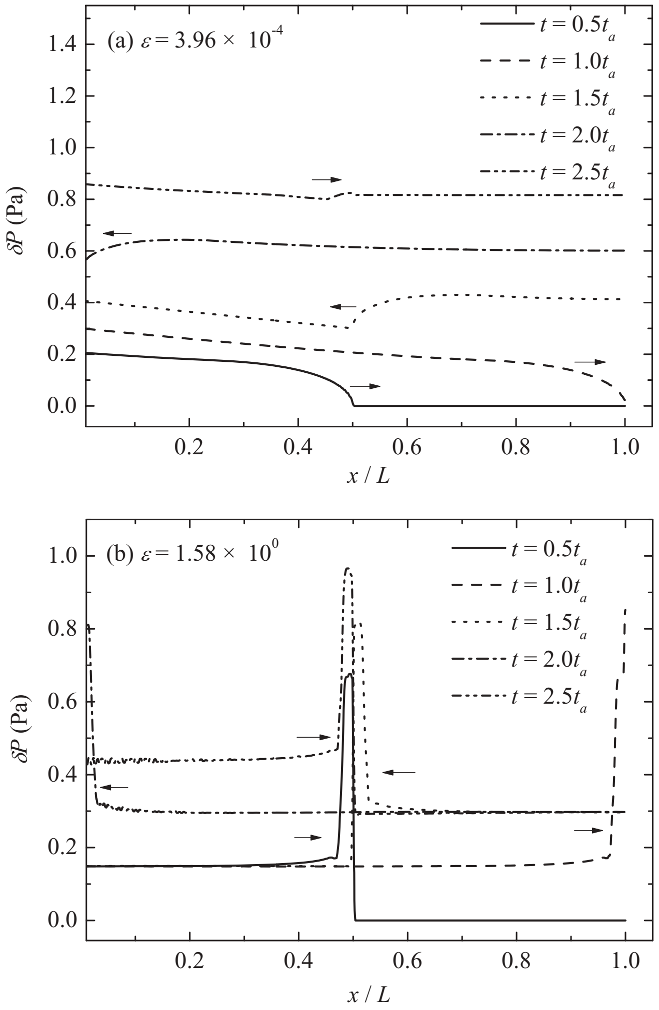

FIG. 7. Spatial pressure profiles at various times under the boundary heating, for (a) $\varepsilon = 3.96 \times 10^{-4}$ and (b) $\varepsilon = 1.58 \times 10^{0}$. Solid curve: $t = 0.5t_a$; dashed curve: $t = 1.0t_a$; dotted curve: $t = 1.5t_a$; dashed-dotted curve: $t = 2.0t_a$; dashed-dotted-dotted curve: $t = 2.5t_a$. The horizontal axes have been scaled by L. The large pressure increases at the boundaries shown in (b) are due to the reflection of the thermoacoustic wave. Despite the large differences in waveform between (a) and (b), the fluid pressure is gradually raised by the sound propagation in both cases. The arrows denote the direction of the wave propagation.

illustrated in the figure, the wave shape gradually evolves from the former to the latter as ε increases.

In Fig. 7, we plot the spatial profiles of the fluid pressure at different times, for $\varepsilon = 3.96 \times 10^{-4}$ and 1.58×10^{0}, respectively. It is shown that, despite the differences in the wavefront structure, the bulk pressure is increased in a way that is quite similar to what is depicted in Fig. 4. That is, the cumulative effect of the thermoacoustic-wave propagation contributes to the gradual elevation of the average pressure in the cell. Moreover, following the eventual stabilization of the boundary pressurization [Fig. 5(b)], the waveform for $\varepsilon = 1.58 \times 10^{0}$ shown in Fig. 7(b) quickly turns flat, similar to that under the linear perturbation [cf. Fig. 4(b)]. It is thus supposed that the nonlinear effect caused by ε depends for the most part on the boundary-layer relaxation, which only lasts as long as the boundary pressure remains unstable. Over time, its impact on the sound generation might be averaged out. More evidence in support of such long-time convergence of the linear and nonlinear responses will be shown in the following discussion with regard to the energy conversion during the acoustic emission.

C. Energy yield of the thermoacoustic process

The thermoacoustic waves carry energy, as is indicated by the temperature and pressure increases caused by the propagating waves (see Figs. 3, 4, 6, and 7). We can measure the wave energy by calculating the energy variation in the bulk [9,32],

$$\Delta E_{\text{bulk}} = \int P \frac{\delta\rho}{\rho} dx, \tag{16}$$

which is due almost exclusively to the thermoacoustic effect as the heat conduction is mainly confined in the boundary layer.

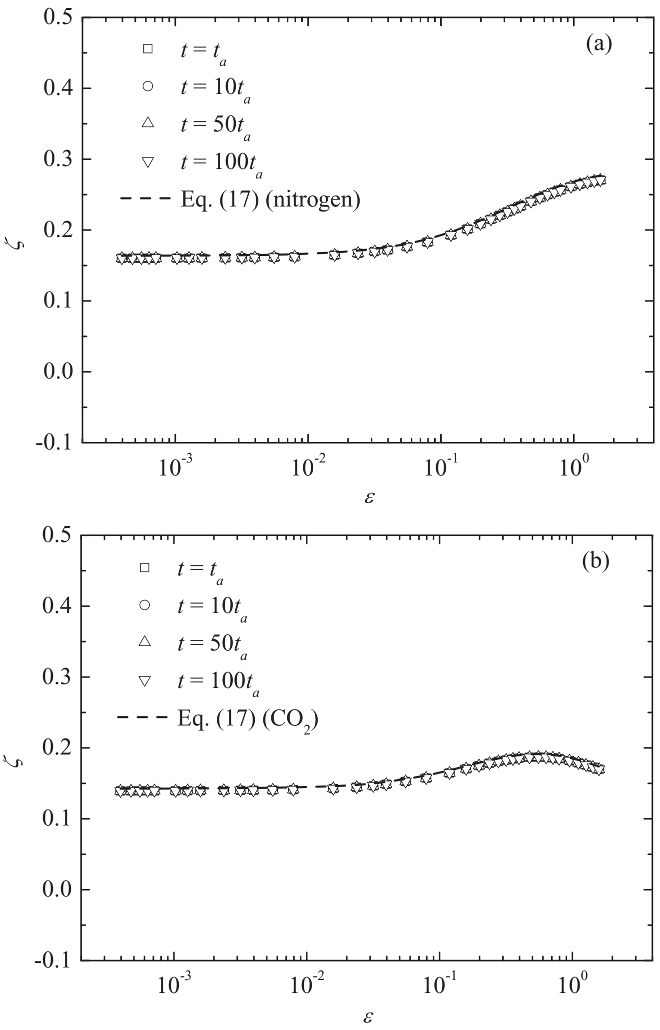

FIG. 8. Calculated energy efficiency ζ vs reduced temperature ε at different times under the internal source heating, in (a) nitrogen and (b) CO_2. Square: $t = t_a$; circle: $t = 10t_a$; up-pointing triangle: $t = 50t_a$; down-pointing triangle: $t = 100t_a$; dashed curve: Eq. (17). The results are presented on a semilogarithmic scale. The calculations are shown to coincide with the theoretical values at all times.

The integration is performed over 99% of the cell except very close to the locus of heating [39].

The ratio $\zeta = E_{\text{bulk}}/Q_{\text{input}}$ represents the energy efficiency of the acoustic emission, through which the mechanical energy is converted from the heat added to the fluid (denoted by Q_{in}). In the case of the internal source heating, the total heat input is evaluated as $Q_{\text{input}} = \int \phi \delta dt$; whereas in the case of the boundary heating, we have $Q_{\text{input}} = \int q_b dt$.

According to the linearized theory [9,18,32], when the boundary layer is sufficiently thin compared to L, the energy efficiency can be approximated by

$$\zeta \simeq \left(1 - \frac{1}{\gamma}\right) \frac{P}{T} \left(\frac{\partial T}{\partial P}\right)_\rho = \left(1 - \frac{1}{\gamma}\right) \frac{P}{T} \frac{\kappa_T}{\alpha_P}. \qquad (17)$$

Close to the CP, the preceding relation is found to tend to a constant.

Figure 8 illustrates the distributions of ζ along the critical isochore at different times based on the numerical simulation under the internal source heating. We plot the results for nitrogen and CO_2, respectively. Also included for comparison are the theoretical predictions by Eq. (17), shown as dashed lines. Exceptionally good agreement can be observed between the simulation and the theory. For both fluids, the results are found to be nearly invariant with time. However, the overall trend of variation of ζ with ε deserves some remarks. It seems from Fig. 8 that the energy efficiency for large ε is ostensibly higher than that for small ε, particularly in the case of nitrogen [Fig. 8(a)]. This observation is somewhat contradictory to the notion that the PE is greatly enhanced approaching the CP. We attempt an explanation here. For any given time, higher ζ means that more energy should be transferred to the bulk via the thermoacoustic process. However, according to Eq. (16), a less conspicuous disturbance to the fluid variables might result from such an energy increase due to the fact that pressure rises significantly with increasing ε along the critical isochore [Eq. (7)]. Also contributing is the rapidly decreasing sound velocity near the CP (see Table I). As a result, the propagating

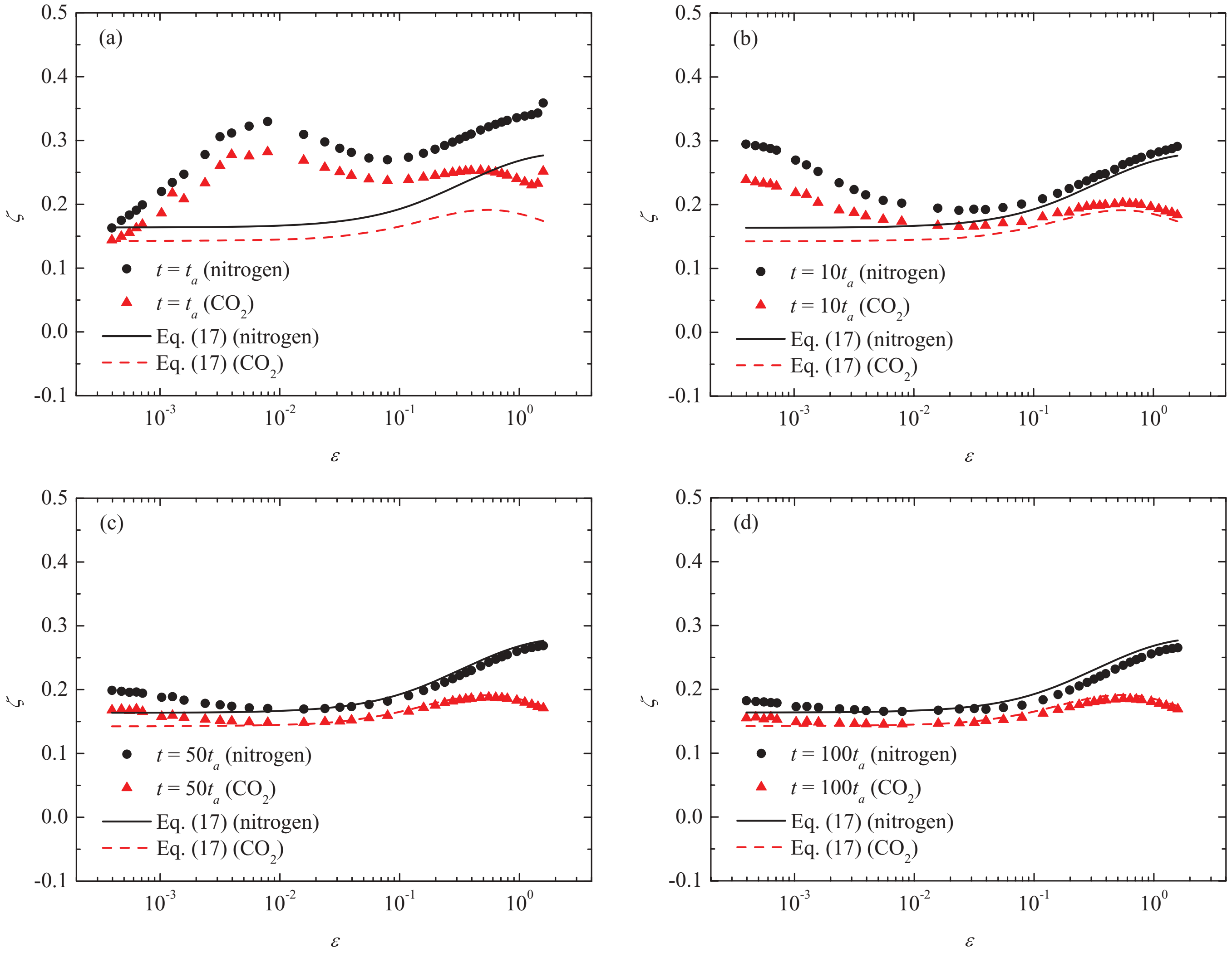

FIG. 9. (Color online) Calculated energy efficiency ζ vs reduced temperature ε in nitrogen and CO_2 under the boundary heating, at (a) $t = t_a$, (b) $t = 10t_a$, (c) $t = 50t_a$, and (d) $t = 100t_a$. Black circle: calculated ζ in nitrogen; red triangle: calculated ζ in CO_2; black solid curve: Eq. (17) for nitrogen; red dashed curve: Eq. (17) for CO_2. The results are presented on a semilogarithmic scale. As time passes, a convergence between the calculations and the theoretical values appears to grow from the right-hand side to the left-hand side of the figures.

thermoacoustic wave could have a larger magnitude when possessing nominally less energy because of the shortened waveform. The thermoacoustic behavior thus appears more "detectable" at the CP.

We show in Fig. 9 the time evolutions of ζ in nitrogen and CO_2 under the boundary heating, and their comparison with Eq. (17), which (according to Fig. 8) amounts to an indirect comparison between the linear and nonlinear cases. In early times, as depicted in Fig. 9(a), significant differences can be found between the predicted energy efficiencies under the internal heating and boundary heating, which correspond with the outstanding waveform deformation with varying ε as shown in Fig. 6. As time goes on, the gaps between the linear and nonlinear cases are getting smaller and smaller. Ultimately, at $t = 100t_a$ [Fig. 9(d)], it seems that a convergence is almost reached for both nitrogen and CO_2. It is interesting to note that, as the figure shows, the merging of the curves appears to start from the points with large ε values and then moves gradually toward the CP. As we have discussed previously, the nonlinear features of the thermoacoustic waves are closely related to the boundary pressure variation. For small ε, it is argued that it takes a considerably long time for the boundary pressure to finally stabilize [Fig. 5(b)]. Consequently, alleviating the differences resulting from the nonlinear effects should require more time.

In spite of being touted as the fourth mode of heat transfer, one of the core premises of the PE, paradoxically, is that the process is strictly adiabatic. Here we define the coefficient ξ as the ratio of the entropy-based heat transport [Eq. (5)] in the bulk of the fluid to the total energy input, which reads

$$\xi = \frac{\int_{\text{bulk}} \rho T \delta s dx}{Q_{\text{in}}} = \frac{\int_{\text{bulk}} dx \left(\rho C_P \delta T - \rho (C_P - C_V) \frac{\kappa_T}{\alpha_P} \delta P\right)}{Q_{\text{in}}}. \quad (18)$$

In Fig. 10, we plot the short-time ($t = t_a$) and long-time ($t = 100t_a$) calculations of ξ versus ε for nitrogen and CO_2, in the linear and nonlinear cases, respectively. Unsurprisingly, ξ is found to be near zero consistently, which attests to the adiabatic nature of the thermoacoustic effect.

Let us end this section by remarking that the use of Eq. (15) in the modeling of the boundary heating suffers from some defects. One of the assumptions of Eq. (15) is that at any given time, the heat input is being completely absorbed by the boundary layer. In using Eq. (15), in effect we neglect the contribution of the acoustic emission. As a result, the boundary temperature could be slightly overestimated. Besides, the errors derived from omitting the temperature variation at the edge of the boundary layer, as Eq. (14) implies, could accrue over time as the bulk temperature is slowly increased by the thermoacoustic coupling. On the other hand, still little is known about the thickness of the thermal boundary layer very close to the CP [40]. The crude generalized treatment of the growth of the boundary layer as $(Dt)^{1/2}$ could introduce some additional uncertainties regarding the results from the boundary heating. These theoretical shortcomings might contribute to the imperfect convergence of ζ [Fig. 9(d)] and the noticeable deviations of ξ near the CP [Fig. 10(b)] at later stages.

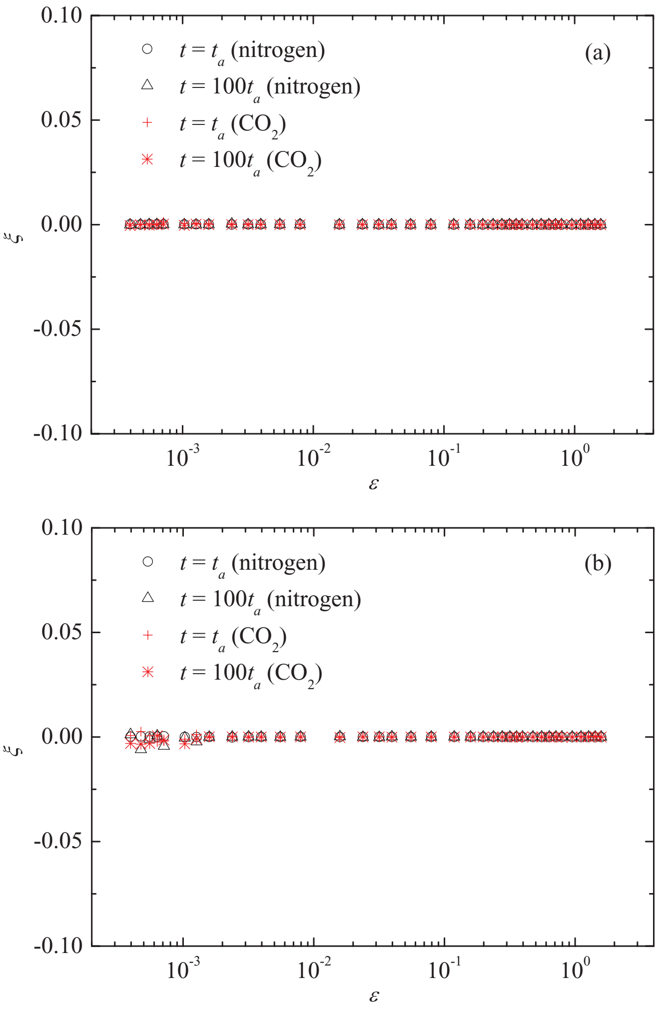

FIG. 10. (Color online) Calculated coefficient ξ vs reduced temperature ε, under (a) the internal source heating and (b) the boundary heating. Black circle: for nitrogen at $t = t_a$; black triangle: for nitrogen at $t = 100t_a$; red cross: for CO_2 at $t = t_a$; red star: for CO_2 at $t = 100t_a$. The results are presented on a semilogarithmic scale. Most of the data spread neatly near zero, despite some deviations arising for small ε in (b).

IV. CONCLUDING REMARKS

In the present work, we have explored the thermoacoustic-wave features over several decades of reduced temperatures along the critical isochore by numerically solving the governing differential equations. Two different types of thermal perturbations (i.e., the internal source heating and boundary heating) have been used in the investigation, through which the fluid is essentially subject to linear and nonlinear boundary-layer temperature changes, respectively. The sound generation is found to be markedly different under these two situations. In the linear case, homogeneous thermoacoustic waves are induced by the heat input, which vary only in strength with the distance to the CP. On the other hand, under the nonlinear temperature disturbance, variation in the thermophysical properties causes serious distortions to the wavefront profile in the early stage. In later times, however, the simulations conducted in nitrogen and CO_2 both suggest that the two cases could gradually converge in terms of the energy yield of the thermoacoustic process, with the impact of the initial nonlinearity being slowly smeared out. The strong adiabatic nature of the thermoacoustic waves is also explicitly confirmed in the analysis.

It should be pointed out that the results of the present study still need further experimental verification. Since the differences between the boundary heating and the internal source heating are both delicate in scale and transient in nature, careful experimental design and accurate measurement are essential for developing a better understanding of thermoacoustic-wave motion.

ACKNOWLEDGMENTS

This research is supported by the National Natural Science Foundation of China under Contract No. 50976068. B.S. acknowledges financial support for the Young Scholar of Distinction of Ph.D. Students from the Ministry of Education of China.

APPENDIX: SOLUTIONS TO THE HEAT CONDUCTION PROBLEM UNDER VARIOUS THERMAL DISTURBANCES

In the classical regime of the PE (not too close to the CP), thermal boundary layers are purely diffusive [33]. We can gain important insights into the boundary-layer dynamics by solving the corresponding heat conduction equation with similar problem configurations. Here we present several examples with formulations that are of particular interest to the present work.

A. Internal heating with an infinitesimal source

Consider a semi-infinite medium ($0 \leqslant x < \infty$) is initially at T_i; for times $t > 0$ there is an infinitesimal heat source located at $x = 0$ releasing energy at a rate of Q_v per unit time per unit volume. No heat flux is allowed to cross the boundary at $x = 0$. Based on the Fourier law, the heat conduction equation is formulated as

$$\frac{\partial T}{\partial t} = D\frac{\partial^2 T}{\partial x^2} + \frac{Q_v}{\rho C_P}\delta(x), \tag{A1}$$

with the initial condition

$$T(x,t=0) = T_i \tag{A2}$$

and the boundary condition

$$\frac{\partial T}{\partial x}(x=0,t) = 0. \tag{A3}$$

Here $\delta(x)$ is the unit Dirac delta function. We introduce the dimensionless excess temperature $\theta(x,t) = (T - T_i)/T_i$, and the preceding equations become

$$\frac{\partial \theta}{\partial t} = D\frac{\partial^2 \theta}{\partial x^2} + \Lambda\delta(x), \tag{A4}$$

$$\theta(x,t=0) = 0, \tag{A5}$$

$$\frac{\partial \theta}{\partial x}(x=0,t) = 0, \tag{A6}$$

with $\Lambda = Q_v/(\rho C_P T_i)$. We use Green's function [41] to solve Eqs. (A4)–(A6). To determine Green's function $G(x,t|x',t')$, we first need to consider the homogeneous auxiliary problem defined through

$$\frac{\partial \phi}{\partial t} = D\frac{\partial^2 \phi}{\partial x^2}, \tag{A7}$$

$$\phi(x,t=0) = F(x), \tag{A8}$$

$$\frac{\partial \phi}{\partial x}(x=0,t) = 0, \tag{A9}$$

where $F(x)$ is the arbitrary initial condition function. The solution is obtained by means of the separation of variables, which yields

$$\phi(x,t) = \int_0^\infty \frac{1}{\sqrt{4\pi Dt}}\left[\exp\left(-\frac{(x+x')^2}{4Dt}\right) + \exp\left(-\frac{(x-x')^2}{4Dt}\right)\right]F(x')dx'. \tag{A10}$$

Based on the Green's function approach, the general solution to the problem (A7)–(A9) can be written as

$$\phi(x,t) = \int_0^\infty G(x,t|x',t')|_{t'=0}F(x')dx'. \tag{A11}$$

Comparing Eq. (A11) with Eq. (A10), with t replaced by $t{-}t'$, leads to

$$G(x,t|x',t') = \frac{1}{\sqrt{4\pi D(t-t')}}\left[\exp\left(-\frac{(x+x')^2}{4D(t-t')}\right) + \exp\left(-\frac{(x-x')^2}{4D(t-t')}\right)\right]. \tag{A12}$$

The temperature solution to the original problem (A4)–(A6) is thus described by

$$\begin{aligned}\theta(x,t) &= \Lambda\int_0^t dt'\int_0^\infty G(x,t|x',t')\delta(x')dx' \\ &= \Lambda\int_0^t \frac{1}{\sqrt{4\pi D(t-t')}}dt' \\ &\quad\times\int_0^\infty\left[\exp\left(-\frac{(x+x')^2}{4D(t-t')}\right) + \exp\left(-\frac{(x-x')^2}{4D(t-t')}\right)\right]\delta(x')dx' \\ &= \Lambda\int_0^t \frac{1}{\sqrt{4\pi D(t-t')}}\exp\left(-\frac{x^2}{4D(t-t')}\right)dt'.\end{aligned} \tag{A13}$$

Set $\tau = t{-}t'$ and the preceding equation becomes

$$\theta(x,t) = \Lambda\int_0^t \frac{1}{\sqrt{4\pi D\tau}}\exp\left(-\frac{x^2}{4D\tau}\right)d\tau. \tag{A14}$$

From Eq. (A14), one finds that the temperature at $x = 0$, due to the internal heat generation, increases at a rate

$$\left.\frac{\partial \theta}{\partial t}\right|_{x=0} = \frac{\Lambda}{\sqrt{4\pi Dt}}. \tag{A15}$$

B. Internal heating with a finite-size source

Now we replace the infinitesimal source with a finite-size source, and keep the rest of the configuration unchanged. The problem can be reformulated as

$$\frac{\partial \theta}{\partial t} = D\frac{\partial^2 \theta}{\partial x^2} + \Lambda \Pi(x), \tag{A16}$$

$$\theta(x,t=0) = 0, \tag{A17}$$

$$\frac{\partial \theta}{\partial x}(x=0,t) = 0, \tag{A18}$$

where instead of the Dirac delta function, the spatial profile of the source is given as

$$\Pi(x) = \begin{cases} 1, & 0 \leqslant x \leqslant \Delta, \\ 0, & x > \Delta. \end{cases} \tag{A19}$$

In Eq. (A19), Δ is the width of the source. Note that such a setup is similar to the case of the internal source heating studied in Sec. III A. Repeating the previously described steps leads to

$$\begin{aligned} \theta(x,t) &= \Lambda \int_0^t dt' \int_0^\infty G(x,t|x',t')\Pi(x')dx' \\ &= \Lambda \int_0^t \frac{1}{\sqrt{4\pi D(t-t')}}dt' \\ &\quad \times \int_0^\Delta \left[\exp\left(-\frac{(x+x')^2}{4D(t-t')}\right)\right. \\ &\quad \left. + \exp\left(-\frac{(x-x')^2}{4D(t-t')}\right)\right]dx' \\ &= \frac{\Lambda}{2}\int_0^t \left[\operatorname{erf}\left(\frac{x+\Delta}{\sqrt{4D(t-t')}}\right)\right. \\ &\quad \left. - \operatorname{erf}\left(\frac{x-\Delta}{\sqrt{4D(t-t')}}\right)\right]dt'. \end{aligned} \tag{A20}$$

Again, substituting τ for t–t' in the equation yields

$$\theta(x,t) = \frac{\Lambda}{2}\int_0^t \left[\operatorname{erf}\left(\frac{x+\Delta}{\sqrt{4D\tau}}\right) - \operatorname{erf}\left(\frac{x-\Delta}{\sqrt{4D\tau}}\right)\right]d\tau, \tag{A21}$$

which, after differentiating with respect to t, becomes

$$\frac{\partial \theta}{\partial t} = \frac{\Lambda}{2}\left[\operatorname{erf}\left(\frac{x+\Delta}{\sqrt{4Dt}}\right) - \operatorname{erf}\left(\frac{x-\Delta}{\sqrt{4Dt}}\right)\right]. \tag{A22}$$

In the limit of $t \to 0$, the time rate of the temperature increase at $x = 0$,

$$\left.\frac{\partial \theta}{\partial t}\right|_{x=0} \simeq \Lambda, \tag{A23}$$

is almost constant. In the early stage, the input energy is nearly completely devoted to heating the fluid at the source, which results in a linear temperature increase.

C. Surface heating with a constant heat flux

A semi-infinite region ($0 \leqslant x < \infty$) is subject to a constant heat flux (denoted by Q_W per unit time per unit area) for $t > 0$ at the boundary. The initial temperature is T_i. The mathematical formulation of the problem is

$$\frac{\partial T}{\partial t} = D\frac{\partial^2 T}{\partial x^2}, \tag{A24}$$

$$\frac{\partial T}{\partial x}(x=0,t) = -\frac{Q_W}{\lambda}, \tag{A25}$$

$$T(x,t=0) = T_i. \tag{A26}$$

Once again, the temperature T is substituted by $\theta(x,t) = (T - T_i)/T_i$, which leads to

$$\frac{\partial \theta}{\partial t} = D\frac{\partial^2 \theta}{\partial x^2}, \tag{A27}$$

$$\frac{\partial \theta}{\partial x}(x=0,t) = -\frac{Q_W}{\lambda T_i} = -\Theta, \tag{A28}$$

$$\theta(x,t=0) = 0. \tag{A29}$$

We split up the nonhomogeneous problem ($\theta = \psi + \varphi$) into a steady problem defined as

$$\frac{d^2\psi}{dx^2} = 0, \tag{A30}$$

$$\frac{d\psi}{dx}(x=0) = -\Theta, \tag{A31}$$

and a homogeneous unsteady problem defined as

$$\frac{\partial \varphi}{\partial t} = D\frac{\partial^2 \varphi}{\partial x^2}, \tag{A32}$$

$$\frac{\partial \varphi}{\partial x}(x=0,t) = 0, \tag{A33}$$

$$\varphi(x,t=0) = -\psi(x). \tag{A34}$$

It can be easily shown that

$$\psi = -\Theta x. \tag{A35}$$

Following the method of separation of variables [41], we obtain the solution to Eqs. (A32)–(A34),

$$\varphi(x,t) = \Theta\left[\sqrt{\frac{4Dt}{\pi}}\exp\left(-\frac{x^2}{4Dt}\right) + x\operatorname{erf}\left(\frac{x}{\sqrt{4Dt}}\right)\right]. \tag{A36}$$

Finally, the temperature distribution of the original problem is found to be

$$\theta(x,t) = \Theta\left[\sqrt{\frac{4Dt}{\pi}}\exp\left(-\frac{x^2}{4Dt}\right) + x\operatorname{erf}\left(\frac{x}{\sqrt{4Dt}}\right) - x\right]. \tag{A37}$$

At $x = 0$, one finds explicitly the temperature variation due to the boundary heat flux,

$$\theta(x=0,t) = \Theta\sqrt{\frac{4Dt}{\pi}}, \tag{A38}$$

which shows the same time dependence of $t^{1/2}$ as is prescribed in the boundary heating case [Eq. (15)].

From Eqs. (A15), (A23), and (A38), it is evident that small subtle adjustments to the problem configuration can bring about different boundary-layer behaviors. In particular, the internal heat generation from a finite-size source causes the temperature to increase linearly as t in early times; whereas the constant boundary heat flux causes the temperature to rise nonlinearly as $t^{1/2}$. The results in Figs 2(a) and 5(a) exhibit similar patterns.

[1] D. R. Kassoy, SIAM J. Appl. Math. **36**, 624 (1979).

[2] A. M. Radhwan and D. R. Kassoy, J. Eng. Math. **18**, 133 (1984).

[3] H. Ozoe, N. Sato, and S. W. Churchill, Chem. Eng. Commun. **5**, 203 (1980).

[4] Y. Huang and H. H. Bau, Int. J. Heat Mass Transf. **38**, 1329 (1995).

[5] Y. Huang and H. H. Bau, Int. J. Heat Mass Transf. **40**, 407 (1997).

[6] M. A. Brown and S. W. Churchill, AIChE J. **41**, 205 (1995).

[7] Y. Lin and B. Farouk, J. Thermophys. Heat Transf. **22**, 105 (2008).

[8] K. Nitsche and J. Straub, in *Proceedings of the 6th European Symposium on Material Science under Microgravity Conditions, Bordeaux, France, 1986* (European Space Agency, Paris,1987), Vol. SP-256, p.109.

[9] A. Onuki and R. A. Ferrell, Physica A **164**, 245 (1990).

[10] A. Onuki, H. Hao, and R. A. Ferrell, Phys. Rev. A **41**, 2256 (1990).

[11] H. Boukari, J. N. Shaumeyer, M. E. Briggs, and R. W. Gammon, Phys. Rev. A **41**, 2260 (1990).

[12] B. Zappoli, D. Bailly, Y. Garrabos, B. Le Neindre, P. Guenoun, and D. Beysens, Phys. Rev. A **41**, 2264 (1990).

[13] H. Boukari, M. E. Briggs, J. N. Shaumeyer, and R. W. Gammon, Phys. Rev. Lett. **65**, 2654 (1990).

[14] P. Guenoun, B. Khalil, D. Beysens, Y. Garrabos, F. Kammoun, B. Le Neindre, and B. Zappoli, Phys. Rev. E **47**, 1531 (1993).

[15] J. Straub and L. Eicher, Phys. Rev. Lett. **75**, 1554 (1995).

[16] B. Bonetti, F. Perrot, D. Beysens, and Y. Garrobos, Phys. Rev. E **49**, R4779 (1994).

[17] T. Fröhlich, P. Guenoun, M. Bonetti, F. Perrot, D. Beysens, Y. Garrabos, B. Le Neindre, and P. Bravais, Phys. Rev. E **54**, 1544 (1996).

[18] Y. Garrabos, M. Bonetti, D. Beysens, F. Perrot, T. Fröhlich, P. Carlès, and B. Zappoli, Phys. Rev. E **57**, 5665 (1998).

[19] A. Nakano, M. Shiraishi, and M. Murakami, Cryogenics **41**, 429 (2001).

[20] H. Boukari, R. L. Pego, and R. W. Gammon, Phys. Rev. E **52**, 1614 (1995).

[21] D. Bailly and B. Zappoli, Phys. Rev. E **62**, 2353 (2000).

[22] A. B. Kogan, D. Murphy, and H. Meyer, Phys. Rev. Lett. **82**, 4635 (1999).

[23] A. B. Kogan and H. Meyer, Phys. Rev. E **63**, 056310 (2001).

[24] A. Furukawa and A. Onuki, Phys. Rev. E **66**, 016302 (2002).

[25] Y. Chiwata and A. Onuki, Phys. Rev. Lett. **87**, 144301 (2001).

[26] S. Amiroudine and B. Zappoli, Phys. Rev. Lett. **90**, 105303 (2003).

[27] G. Accary, I. Raspo, P. Bontoux, and B. Zappoli, Phys. Rev. E **72**, 035301(R) (2005).

[28] S. Amiroudine, P. Bontoux, P. Larroudé, B. Gilly, and B. Zappoli, J. Fluid Mech. **442**, 119 (2001).

[29] B. Zappoli and P. Carlès, Eur. J. Mech. B/Fluids **14**, 41 (1995).

[30] P. Carlès, Phys. Fluids **18**, 126102 (2006).

[31] B. Shen and P. Zhang, Int. J. Heat Mass Transf. **53**, 4832 (2010).

[32] Y. Miura, S. Yoshihara, M. Ohnishi, K. Honda, M. Matsumoto, J. Kawai, M. Ishikawa, H. Kobayashi, and A. Onuki, Phys. Rev. E **74**, 010101(R) (2006).

[33] P. Carlès, Phys. Fluids **10**, 2164 (1998).

[34] P. Carlès and K. Dadzie, Phys. Rev. E **71**, 066310 (2005).

[35] P. Zhang and B. Shen, Phys. Rev. E **79**, 060103(R) (2009).

[36] C. A. J. Fletcher, *Computational Technique for Fluid Dynamics* (Springer-Verlag, Berlin, 1988), vol. **2**.

[37] T. J. Poinsot and S. K. Lele, J. Comput. Phys. **101**, 104 (1992).

[38] We use Eq. (15) as a compromise between computational feasibility and physical accuracy. Simply discretizing Eq. (12) with $\triangle x$ would lead to poor estimation of the boundary temperature because, on the acoustic time scale, the boundary-layer thickness is orders of magnitude smaller than $\triangle x$. Decreasing $\triangle x$ too aggressively near the boundary, on the other hand, would imperil the overall computational stability due to the numerical scheme being explicit.

[39] This might introduce additional errors, which are considered marginal as the results compare exceptionally well with the theory in the linear case (see Fig. 8).

[40] K. A. Gillis, I. I. Shinder, and M. R. Moldover, Phys. Rev. E **70**, 021201 (2004).

[41] M. N. Özişik, *Heat Conduction*, 2nd ed. (Wiley, New York, 1993).